Aerosol-optics model for the backscatter depolarisation ratio of mineral dust particles

Journal of Quantitative Spectroscopy & Radiative Transfer 254 (2020) 107177

Contents lists available at ScienceDirect

Journal of Quantitative Spectroscopy & Radiative Transfer

journal homepage: www.elsevier.com/locate/jqsrt

Aerosol-optics model for the backscatter depolarisation ratio of mineral dust particles

Michael Kahnert[a,b,*], Franz Kanngießer[b], Emma Järvinen[c], Martin Schnaiter[d]

[a] Research Department, Swedish Meteorological and Hydrological Institute, Folkborgsvägen 17, SE-601 76 Norrköping, Sweden
[b] Department of Space, Earth and Environment, Chalmers University of Technology, SE-412 96 Gothenburg, Sweden
[c] National Center for Atmospheric Research (NCAR), Boulder, CO, USA
[d] Karlsruhe Institute of Technology, Hermann-von-Helmholtz-Platz 1, 76344 Eggenstein-Leopoldshafen, Germany

ARTICLE INFO

Article history:
Received 29 April 2020
Revised 17 June 2020
Accepted 18 June 2020
Available online 26 June 2020

Keywords:
Atmospheric optics
Aerosol
Mineral dust
Depolarization

ABSTRACT

The size-dependence of the linear depolarisation ratio of mineral dust aerosols is investigated. Laboratory measurements on 131 different aerosol samples with varying size distributions and mineralogical compositions are fitted with a homogeneous spheroid model. A minimum-bias and minimum-variance fit of the data is obtained for prolate model particles with a refractive index of 1.525+0.001i and an aspect ratio of 0.87. The model error is analysed by varying the input parameters to the light-scattering computations. It is found that the scattering of the measurements about the model can mainly be explained by variation of the morphology and dielectric properties, and to a much lesser extent by variation in the geometric standard deviation of the size distribution. The modelling of the data is extended by using size-shape distributions of spheroids. The results indicate that there is some freedom in choosing the best-fit weights of the shape-distribution of spheroids, which could potentially be useful when extending the model to multiple wavelengths, or to including additional optical parameters other than depolarisation. However, it is also found that the most reasonable fits of the data are obtained by mildly aspherical prolate and oblate spheroids, which limits the freedom of adjusting the best-fit weights.

1. Introduction

Polarimetric observations of aerosols have been applied to retrieve information on aerosol size and refractive index (e.g. [1]) and for providing retrieval products that can be assimilated into chemical transport models (e.g. [2]). The depolarisation ratio obtained from lidar observations is believed to contain a wealth of information that could be exploited for aerosol speciation (e.g. [3,4]). Field observations present a remarkably homogeneous picture for mineral dust aerosols with most observed depolarisation ratios lying in the range 0.30–0.35, as indicated in Tab. 1. By contrast, modelling studies suggest that even minor, seemingly trivial changes in aerosol morphology and composition can result in a substantial variation in the depolarisation ratio of nonspherical particles [5–7]. Thus theoretical models that could provide a basis for a forward model in retrieval methods or chemical data assimilation algorithms come with a substantial error variance, which limits the amount of quantitative information that can be extracted from such measurements (e.g. [8]). This complicates the interpretation and inversion of depolarisation measurements. Therefore, depolarisation is often only used for making a rough qualitative classification of aerosols into fairly broad categories, such as “clean continental”, “polluted continental”, “clean marine”, “polluted dust”, etc[9]. It is rather difficult to make use of such an ad hoc classification in quantitative contexts, such as chemical data assimilation.

There have been numerous studies that tried to reconcile models and measurements for mineral dust aerosols with a focus on the angular distribution of the scattered radiance and polarisation. Most notably, the Amsterdam-Granada light scattering database provides measurements of the full Mueller matrix for a significant number of mineral aerosols and cosmic dust analogues ([19]). The measurements have been reproduced with model computations using spheroids [20,21], polyhedral prisms [20,21], Gaussian random spheres [22], and ellipsoids [23]. In general, spheroids and ellipsoids proved to be the most versatile model, mainly because that class of model particles covers a much broader range of different Mueller matrices than any other model tested [21,24]. Thus, it

* Corresponding author.
E-mail address: michael.kahnert@smhi.se (M. Kahnert).

https://doi.org/10.1016/j.jqsrt.2020.107177

Table 1
Values of linear depolarisation ratio at 532 nm, as reported from lidar field observations.

location	type	δ_l(532 nm)	reference
Midwest US	Saharan dust	0.304 ± 0.005	[10]
Caribbean	Saharan dust	0.327 ± 0.018	[10]
Chihuahuan desert	North American dust	0.373 ± 0.014	[10]
Pico de Orizaba	North American dust	0.334 ± 0.018	[10]
Praia, Cape Verde	Saharan dust	0.30 ± 0.01	[11]
Lampedusa, Italy	Saharan dust	0.30 ± 0.02	[12]
Tokyo, Japan	Asian dust	~ 0.20	[13]
between Bermuda and St. Croix, Virgin Islands	Saharan dust	~ 0.33	[14]
Praia, Cape Verde	Saharan dust	0.32 ± 0.03	[15]
Atlantic Ocean	Saharan dust	0.29 ± 0.01	[16]
Atlantic Ocean	Saharan dust	0.31	[17]
Dushanbe, Tajikistan	Middle Eastern dust	0.31 ± 0.01	[18]
Dushanbe, Tajikistan	Central Asian dust	0.35 ± 0.01	[18]

is often possible to find a size-shape distribution of spheroids that provides a good fit of the Mueller matrix elements of mineral dust aerosols observed in the laboratory. Specifically, the phase function of the feldspar sample in that data base has been used to validate the kernels constructed for AERONET retrievals, which are based on spheroidal model particles [25]. However, it was also demonstrated that there is no single shape distribution of spheroids that works equally well for all mineral dust samples [26]. The AERONET kernel look-up tables contain 11 discrete spheroid aspect ratios; the probability distribution of those can be freely adjusted. This gives the scattering kernels a significant number of free parameters.

Modelling polarimetric differential scattering properties of aerosols is even more challenging than modelling radiometric properties. Here, we want to focus on the linear depolarisation ratio observed in the backscattering direction. Such measurements are available for ground-based [3] and airborne lidar measurements [10] as well as from space-borne sensors, such as CALIOP/CALIPSO [27], CATS [28] and ATLID [29,30]. Numerous models can be used to simulate optical properties of irregular aerosols, such as mineral dust (e.g. [31]). However, in large-scale applications, such as in remote sensing and chemical data assimilation, computational limitations often constrain us to using simple model particles, i.e., particles with a high degree of symmetry [32,33]. Owing to their high flexibility, we will focus on homogeneous spheroids. Rather than constructing kernel look-up tables with a large number of free parameters, our goal is to constrain the shape distribution of the spheroidal model particles by use of laboratory measurements [34]. Also, rather than focusing on only a few more or less representative measurements, our approach is based on considering a large number of mineral dust samples with varying composition and size distributions. Our main hypothesis is that one can find a spheroid or a shape-distribution of spheroids that reproduces the observed size dependence of the depolarisation ratio of mineral aerosols. Clearly, we do not expect to find a simple model that will fit the depolarisation of each and every sample. Rather, we aim at finding a manifestation of the simple spheroid model that fits the observations with a reasonably small bias and standard deviation. Further, we hypothesise that we should be able to explain the standard deviation of the observations relative to our model by varying input parameters to the computations (refractive index, morphology, and size variance) within reasonable limits.

The data as well as the numerical methods employed in this work will be introduced in Sect. 2. Results and discussions are given in Sects. 3 and 4, respectively. Concluding remarks are found in Section 5.

2. Methods

2.1. Measurements

Laboratory measurements of near-backscattering (178°) linear depolarisation ratios of over 131 different dust samples were performed in the aerosol and cloud simulation chamber AIDA of Karlsruhe Institute of Technology. The optical measurements were conducted with two scattering and depolarisation instruments (SIMONE, [34,35]) operating at slightly different wavelengths of 488 and 552 nm.

Both SIMONE instruments consist of a sender and receiver units. The sender unit has a continuous-wave (cw) laser that is directed across the chamber. The polarisation state of the laser can be modified between vertical and horizontal linear polarisation using liquid crystals. In the experiments, horizontal polarisation is usual. The receiver unit consists of a telescope assembly, a polarization prism and two detectors. The linear depolarisation ratio is defined as the ratio between the cross-polarised and co-polarised signals and can be expressed by

$$\delta_l(\Theta) = \frac{1 - F_{22}/F_{11}}{1 + 2F_{12}/F_{11} + F_{22}/F_{11}}, \tag{1}$$

where F_{ij} $(i, j = 1, \ldots, 4)$ are the elements of the Stokes scattering matrix, which express the linear relation between the four-component Stokes vectors of the incident and the scattered radiation.

The AIDA chamber consists of a large (84 m^3) vessel that allows a long residence time for aerosols and, thus, stable conditions for measurement of aerosol optical properties. Dust samples used in the chamber experiments included desert dust samples from the Sahara, Asia and Afghanistan, soil dust samples from Mongolia, Argentina and Germany as well as artificially prepared samples, including Arizona test dust, kaolinite, illite and hematite. We excluded the hematite samples from the analysis, since the refractive index of this mineral is highly unrepresentative of atmospheric mineral aerosols. The samples were prepared using cyclones with different cutoff to achieve different maximum diameters, and introduced to the chamber using a rotating brush generator that reduced the maximum dust particle diameter to approximately 10 µm. The size distribution of the dust in the chamber was measured with a combination of an aerodynamic particle sizer (APS) and scanning mobility particle sizer (SMPS). This procedure resulted in mono-modal aerosol populations with median volume-equivalent radii ranging from 0.12 to 1.9 µm, or size parameter ranging from 1.6–25. (The size parameter is defined as $x = 2\pi r/\lambda$, where r is the volume-equivalent radius of the particles, and λ is the wavelength of light.) The mode widths (σ) were in the range from 1.35 to 2.32.

A more detailed description of the instruments, the experimental procedure and the dust samples can be found in [34].

2.2. Model particles

The main motivation of this work was to find a model particle that is simple enough to be used in inverse problems, specifically in chemical data assimilation. Our main hypothesis was that spheroids can be employed for representing the size dependence of the depolarisation ratio of mineral dust. Thus, the reference geometry in our computations were spheroids. However, inverse models also require error estimates for the forward model that is being employed for solving the inverse problem. Therefore, we also investigated the effect of uncertainties in the input parameters to the optics model on the model output. Specifically, to estimate the sensitivity of depolarisation to a variation in particle morphology, we perturbed the spheroid geometry with a Gaus-

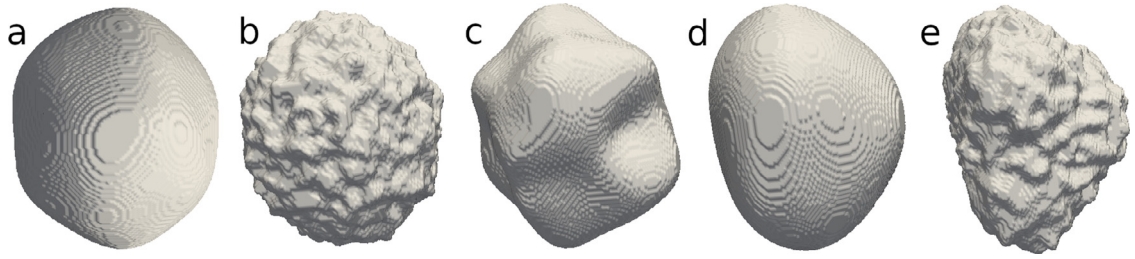

Fig. 1. Five different models of Gaussian random spheroids used in estimating the error variance of the spheroid model. The models differ in their radial standard deviation and correlation angles, as indicated in the text. Models (a)–(d) are characterised by a single roughness scale, while model (e) has two superimposed roughness scales.

sian random distortion. Surface roughness [36], and in particular irregular surface distortions are known to have potentially significant effects on optical properties (e.g. [37]). Originally, the Gaussian random sphere (GRS) was constructed by randomly perturbing the surface of a sphere with a prescribed relative radial standard deviation $\sigma_{\rm r}$ and correlation angle γ [38]. We adapted the code G-sphere for generating GRS geometries in order to generate Gaussian random spheroids. More specifically, given the surface parameterisation $r_{\rm spheroid}(\theta)$ of a spheroid with prescribed volume-equivalent radius and aspect ratio, and given the surface parameterisation $r_{\rm GRS}(\sigma_{\rm r},\,\gamma;\,\theta,\,\phi)$ of a *unit* Gaussian random sphere with prescribed $\sigma_{\rm r}$ and γ, we simply defined the surface parameterisation of a Gaussian random spheroid by

$$r(\theta,\phi) = r_{\rm spheroid}(\theta)\cdot r_{\rm GRS}(\sigma_{\rm r},\gamma;\theta,\phi). \tag{2}$$

We further made modifications to superimpose two surface perturbations characterised by two different roughness scales ($\sigma_{\rm r1}$, γ_1) and ($\sigma_{\rm r2}$, γ_2). To this end, we took two unit Gaussian random spheres with surface parameterisations $r_{\rm GRS}(\sigma_{\rm r1},\,\gamma_1;\,\theta,\,\phi)$ and $r_{\rm GRS}(\sigma_{\rm r2},\,\gamma_2;\,\theta,\,\phi)$, and we defined a spheroid with double-roughness scales according to

$$r(\theta,\phi) = r_{\rm spheroid}(\theta)\cdot r_{\rm GRS}(\sigma_{\rm r1},\gamma_1;\theta,\phi)\cdot r_{\rm GRS}(\sigma_{\rm r2},\gamma_2;\theta,\phi). \tag{3}$$

In either case, the particle was represented in the DDA by an array of dipoles. The volume-equivalent radius of the Gaussian random spheroid can be determined by counting the dipoles of the particle, where the volume occupied by each dipole is dependent on the dipole spacing. For small values of the relative radial standard deviation, the volume-equivalent radius is close to that of the unperturbed spheroid.

In our calculations we used five different Gaussian random spheroid models that are illustrated in Fig. 1.

The first four geometries (a)–(d) represent spheroids with a single roughness scale, while geometry (e) has been made by superimposing two different Gaussian random surface perturbations. More specifically, the radial standard deviation and correlation angles used to generate these particles were:

(a) $\sigma_{\rm r} = 0.03,\ \gamma = 20^\circ$.
(b) $\sigma_{\rm r} = 0.03,\ \gamma = 4^\circ$.
(c) $\sigma_{\rm r} = 0.10,\ \gamma = 20^\circ$.
(d) $\sigma_{\rm r} = 0.10,\ \gamma = 40^\circ$.
(e) $\sigma_{\rm r1} = 0.20,\ \gamma_1 = 40^\circ,\ \sigma_{\rm r2} = 0.03,\ \gamma_2 = 4^\circ$.

Thus, (a) and (b) allowed us to compare a small-amplitude surface perturbation with large and small correlation angle; (a) and (c) allowed us to compare a small-amplitude and a large-amplitude perturbation with equal correlation angle; (c) and (d) represented two perturbations with equally large amplitude and different correlation angles. Finally, particle (e) had one surface perturbation with a large standard deviation and correlation angle, and a small-scale surface roughness with a small standard deviation and correlation angle. For each of these five models, we performed computations for five stochastic realisations of the geometry.

Inhomogeneity and porosity can impact optical properties of aerosols (e.g. [6,39,40]). Therefore, we also considered the effect of inhomogeneous mineralogical composition by performing computations for spheroids with randomly-placed spherical hematite inclusions. For reasons that will become clear in Sect. 3.2, we took a refractive index of $m = 1.525 + 0.001i$ as a reference. Using Maxwell Garnett effective medium theory [41], this corresponds to a mixture of a non-absorbing mineral with m_1=1.5128 + 0i, and 0.74% hematite with m_2=3.0 + 0.1i. Thus we constructed inhomogeneous particles by randomly placing spherical hematite inclusions inside a non-absorbing host spheroid with m_1=1.5128 + 0i. The volume fraction f and the maximum size parameter $x_{\rm a,max}$ of the spherical inclusions was prescribed, while the number of inclusions was adjusted accordingly. We set f=0.74%, and we used two values of $x_{\rm a,max}$, namely, 0.3 and 0.4. For each of these two inclusion sizes we generated 5 different stochastic realisations of the randomly placed inclusions. Thus, for each particle size, the ensemble consisted of 10 different morphologies. Note that the fairly low value of f limits the maximum possible inclusion size. Also, it makes little sense to decrease $x_{\rm a,max}$ below 0.3, because this would bring us into the range of applicability of effective medium theories, where the optical properties of inhomogeneous particles become indistinguishable from those of homogeneous particles with a corresponding effective refractive index [6,40].

2.3. Light scattering computations

In a first step, we considered optical properties of spheroids over a large range of refractive indices, sizes, and aspect ratios. More specifically, we considered optical properties averaged over mono-modal lognormal size distributions with a median size parameter ranging between 1–20. The refractive index was varied over the range from $m = n + i\kappa$=1.5+0i to 1.6+0.01i, where m denotes the complex refractive index, and n and κ denote its real and imaginary part, respectively. (Actually, we also considered higher values of n and κ, but the results strongly deviated from the measurements. Therefore, we do not present these results here.)

The goal of this prospecting study was to narrow down the range of aspect ratios and refractive indices that yield depolarisation ratios in a similar range as the laboratory measurements. Covering a large parameter range involves time-consuming computations. To circumvent these problems, we employed pre-computed optical properties from the SCATDB database [42]. The optical properties were averaged over log-normal size distributions representative of the measured samples, as explained in Sect. 3.2. A limitation of the SCATDB version we had access to was that the database only contained cross-polarisation data in the exact backscattering direction, while the laboratory measurements have been performed at a scattering angle of 178°. As we will see in Section 3.2, this was no serious limitation for this first prospecting step. However, once we had narrowed down the range of reasonable particle shapes and refractive indices, we needed to perform more detailed computations at the exact scattering angle of 178°.

To this end, we computed optical properties of homogeneous spheroids for a narrower range of aspect ratios and refractive indices by use of the T-matrix code described in [43]. This code solves the light scattering program by use of Waterman's null-field method [44]. We mainly used the double-precision version of the code (with the exceptions noted below) in conjunction with the LAPACK LU decomposition routines. The program contains automatic routines for ensuring the convergence of the numerical solution. It also contains an implementation of an analytical method for averaging optical properties over particle orientations [45]. Size-averaging of optical properties was performed over the size range 0.025 μm $\leq r \leq$ 3.104 μm, where r denotes the volume-equivalent radius. This range goes up to the maximum size parameter $x = 40$ at 488 nm wavelength that is included in SCATDB.

Once we had found a spheroid model that reproduces the laboratory observations, we needed to obtain an estimate of the model uncertainties. To this end, we studied the sensitivity of the computed depolarisation ratio to a variation in the input parameters, such as the refractive index, the spheroids' aspect ratio, the variance of the size distribution, as well as to deviations from the idealised spheroidal shape. For the latter, we considered irregular and inhomogeneous particles, as explained in Sect. 2.2.

Optical properties of Gaussian random spheroids and inhomogeneous spheroids were calculated by use of the discrete dipole approximation (DDA). Owing to the high computational demands we split the computations between two clusters. The Gaussian random spheroids as well as the inhomogeneous spheroids with size parameters $x \geq 15$ were run on the Bi cluster at the National Supercomputer Centre at Linköping University. The cluster consists of 8-core Intel Xeon E5-2640v3 processors at 2.6 GHz. The inhomogenous spheroids with $x < 15$ were run on the cluster Vera at the Chalmers Centre for Computational Science and Engineering. The calculations on the Vera cluster were run on 64-core (of which 32 cores were virtual cores due to hyperthreading) Intel Xeon Gold 6130 processors at 2.1 GHz. At Chalmers we have installed the ADDA program (version 1.2) [46]. On Bi we have installed the DDSCAT program (Version 7.3.2) [47], in which the user needs to specify the number of discrete orientations over which the optical properties will be averaged, as well as the dipole spacing d. It is usually recommended to choose d such that $|m|kd \leq 0.5$, where m is the complex refractive index of the material, and k is the wavenumber in vacuum.

We tested the convergence of the DDSCAT solution with respect to both d and the number of orientational angles. To this end, we compared DDA computations for randomly oriented homogeneous spheroids to numerically exact benchmark computations obtained with the T-matrix program by Mishchenko et al. [43]. The test spheroids had a refractive index m=1.57 + 0.003i and an aspect ratio of a/b=3.0. Here b denotes the extent along the spheroid's main rotational symmetry axis, and a is the maximum extent perpendicular to that axis.

First, the number of orientational angles was varied. The spheroid was tilted by a polar angle and rotated by an azimuthal angle. We varied the number of discrete polar and azimuthal angles over which the optical properties were averaged until convergent results were obtained. Second, we varied the dipole spacing such that $|m|kd$ assumed the values 0.15, 0.30, and 0.5.

We tested all elements of the Stokes scattering matrix, but in Fig. 2 we only show the element F_{22}/F_{11}. This element is the most sensitive indicators for testing convergence. The element F_{12}/F_{11}, which also contributes to δ_l in Eq. (1), is very close to zero in the near-backscattering direction. In the left panel of Fig. 2 the T-matrix reference results (black) are compared to DDA computations based on averaging over 144 (blue) and 288 (red) discrete particle orientations. The dipole spacing was set to $|m|kd$=0.3. The DDA results agree with the T-matrix results up to scattering angles of about 75°. At larger angles, the results averaged over 288 discrete angles agree reasonably well with the reference results, while those averaged over 144 discrete angles deviate noticeably, especially at scattering angles around 100° and 140°. We are particularly interested in the linear depolarisation ratio. In the backscattering direction, the reference computation give us $\delta_l(\pi)$=0.70. The corresponding DDA results for 144 and 288 angles are $\delta_l(\pi)$=0.67 and 0.68, respectively. A further increase in the number of orientational angles had little effect on the accuracy of the results. We conclude that 288 angles are sufficient for computing the orientationally-averaged depolarisation of spheroids. The remaining discrepancy between the reference and DDA results is mainly due to the finite dipole spacing. Note that non-axisymmetric particles require averaging over an additional Euler angle. For non-axisymmetric particles, we numerically averaged DDA results over a total of 6912 discrete angles.

The error caused by a finite dipole spacing is investigated in the right panel of Fig. 2. The reference results (black) are compared to DDA results, which were averaged over 288 discrete orientations, and computed for dipole spacings $|m|kd$=0.50 (green), 0.30 (blue), and 0.15 (red). The DDA results converge toward the T-matrix results as the dipole spacing is reduced. The corresponding values of $\delta_l(\pi)$ for the DDA results are 0.65, 0.68, and 0.69, which should be compared to the reference results of 0.70. Thus the corresponding relative errors in $\delta_l(\pi)$ are 7.1%, 2.9% and 1.4% for $|m|kd$=0.50, 0.30, and 0.15, respectively. We considered a relative error of 3–5% acceptable for our purposes, since we only performed DDA computations for obtaining error estimates. Thus, we performed all DDA computations for size parameters up to x=15 for a dipole spacing of $|m|kd$=0.30. For larger size parameters, we used $|m|kd$=0.40.

For a few selected cases we ran both DDSCAT and ADDA and found perfect agreement of the results (not shown).

Finally, we investigated the prospects of fitting the observations with a size-shape distribution of spheroids. To this end, we computed size-averaged optical properties with the same T-matrix code [43] for an extended range of aspect ratios, namely, a/b=0.5, 0.67, 0.77, 0.87, 1.0, 1.15, 1.3, 1.5, 2.0. For 0.67 $\leq a/b \leq$ 1.5 we used the double-precision version of the T-matrix code. For a/b=0.5 and 2.0 the extended-precision version was used. The shape distribution of the spheroids that best reproduced the measurements was determined by a least-squares fit of the data, using the lmfit package in python.

3. Results

3.1. Size distribution of the mineral dust samples

For each mineral sample studied in the AIDA chamber, the size distribution (SD) was measured and fitted by use of a log-normal distribution function

$$n(r) = \frac{1}{r \ln \sigma_n \sqrt{2\pi}} \exp\left[-\frac{\ln^2(r/r_0)}{2 \ln^2 \sigma_n}\right]. \quad (4)$$

Here r is the volume-equivalent radius of the particles, r_0 is the median radius, and σ_n represents the geometric standard deviation.

Fig. 3 shows the geometric standard deviation σ_n^{obs} of the size distributions as a function of the median volume-equivalent radius r_0 (represented by the pluses). There is a very weak upward trend in the data points. A linear fit gave

$$\sigma_n(r_0) = 1.576 + 0.154\, r_0. \quad (5)$$

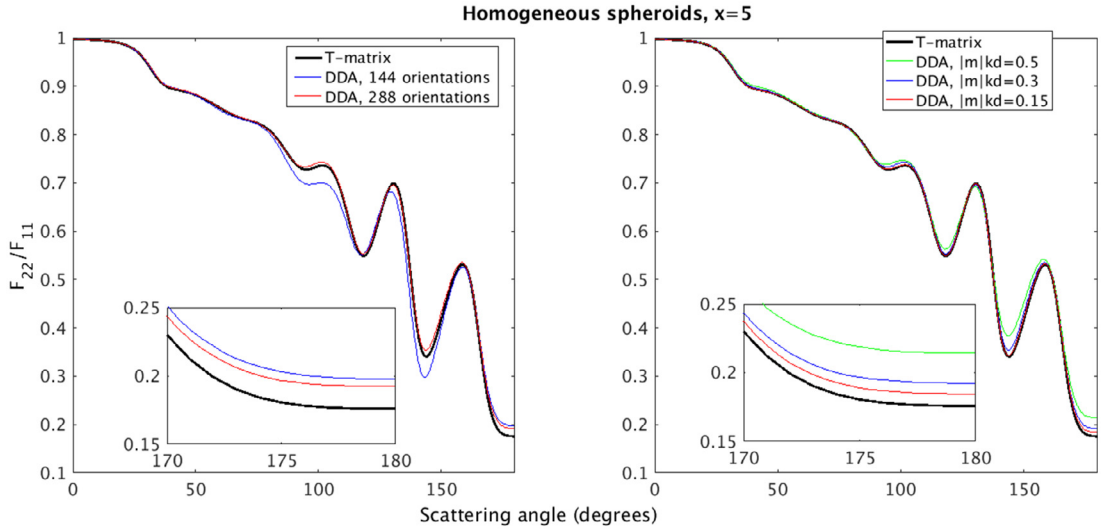

Fig. 2. Element F_{22}/F_{11} of the Stokes scattering matrix computed for randomly oriented homogeneous spheroids with a size parameter $x = 5$. T-matrix reference computations are shown in black. Left panel: DDA computations numerically averaged over a variable number of discrete orientations are shown in blue and red. Right panel: DDA computations for decreasing dipole spacing $|m|kd$ are shown in green, blue, and red. (For interpretation of the references to colour in this figure legend, the reader is referred to the web version of this article.)

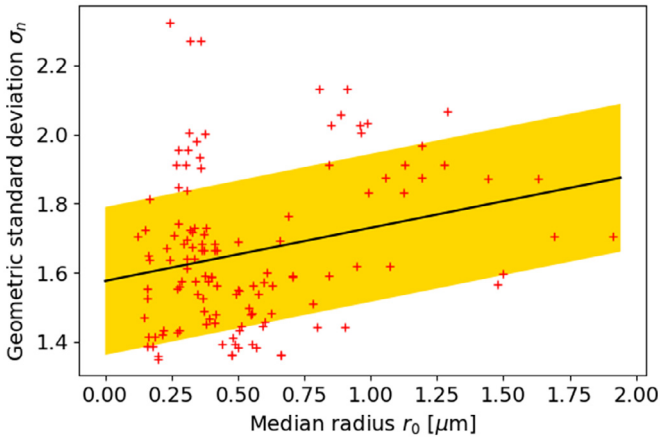

Fig. 3. Geometric standard deviation σ_n of the lognormal size distribution as a function of median radius r_0. The pluses represent the measured aerosol samples. The black line shows the linear fit of the data, the shading represents the standard deviation σ_s of the data with respect to the linear fit.

The data points $\sigma_n^{\rm obs}$ scatter significantly about this linear fit. We can compute a standard deviation

$$\sigma_s = \sqrt{\frac{1}{N}\sum_{i=1}^{N}(\sigma_n^{\rm obs}(r_i) - \sigma_n(r_i))^2}, \tag{6}$$

where the sum extends over all N observation points. This yields σ_s=0.214. The linear fit $\sigma_n(x) \pm \sigma_s$ is represented by the solid line and the shaded region in Fig. 3

In the aerosol optics computations we averaged the optical properties over log-normal size distributions with various values of r_0. For each r_0 we used Eq. (5) to model the corresponding geometric standard deviation $\sigma_n(r_0)$. To estimate the error introduced by the simple fitting formula in Eq. (5), we also computed size-averaged optical properties for log-normal distributions with geometric standard deviations $\sigma_n(r_0) + \sigma_s$ and $\sigma_n(r_0) - \sigma_s$.

3.2. Fitting AIDA data with spheroids

The first step was to extract and size-average optical properties of spheroids from SCATDB over the selected range of particle sizes and refractive indices. Fig. 4 shows the resulting linear depolarisation ratio in the backscattering direction. On the x-axis, the particle size is expressed by the median size parameter $x_0 = 2\pi r_0/\lambda$. The geometric standard deviation of the size distribution was modelled with Eq. (5). The aspect ratio of the spheroids is shown on the y-axis. The eight different panels show results obtained for different values of the refractive index m, where the real part n increases downwards through rows, while the imaginary part κ increases to the right through columns, as indicated in the panel headings. To facilitate comparison with the observations, Fig. 5 shows a few selected cases from Fig. 4 (as indicated in the legend and panel headings) and compares the model results to the measurements (pluses).

Inspection and comparison with the measurements allows us to significantly narrow down the range of plausible aspect ratios. For instance, we see that for mildly oblate spheroids ($a/b > 1$) the depolarisation ratio displays a rather slow upward trend with increasing size parameter, which does not reproduce the size dependency of the observed depolarisation ratios. On the other hand, for $0 \le x \le 5$ prolate spheroids ($a/b < 1$) that deviate strongly from spherical shape show a characteristic rapid increase in the depolarisation ratio with size, which is not found in the measurements. Similar failures in an attempt to fit the observations with spheroids were noted earlier [34]. However, we also see that there is a fairly narrow range of aspect ratios around a/b=0.87 where the model behaviour is very similar to that of the measurements. Thus we performed detailed computations for a more narrowly focused range of input parameters, but with a finer resolution for intermediate values of the refractive index.

We ran the T-matrix code described in [43] for n=1.500, 1.525, 1.550, 1.575, 1.600, for κ=0.000, 0.001, 0.005, 0.010, and for ratios a/b=0.77, 0.87, and 0.93. For each refractive index and aspect ratio we compared the computed depolarisation ratios at Θ=178° to the observed values and computed the bias

$$B = \frac{1}{N}\sum_{i=1}^{N}(\delta_i^{\rm obs} - \delta_i^{\rm mod}), \tag{7}$$

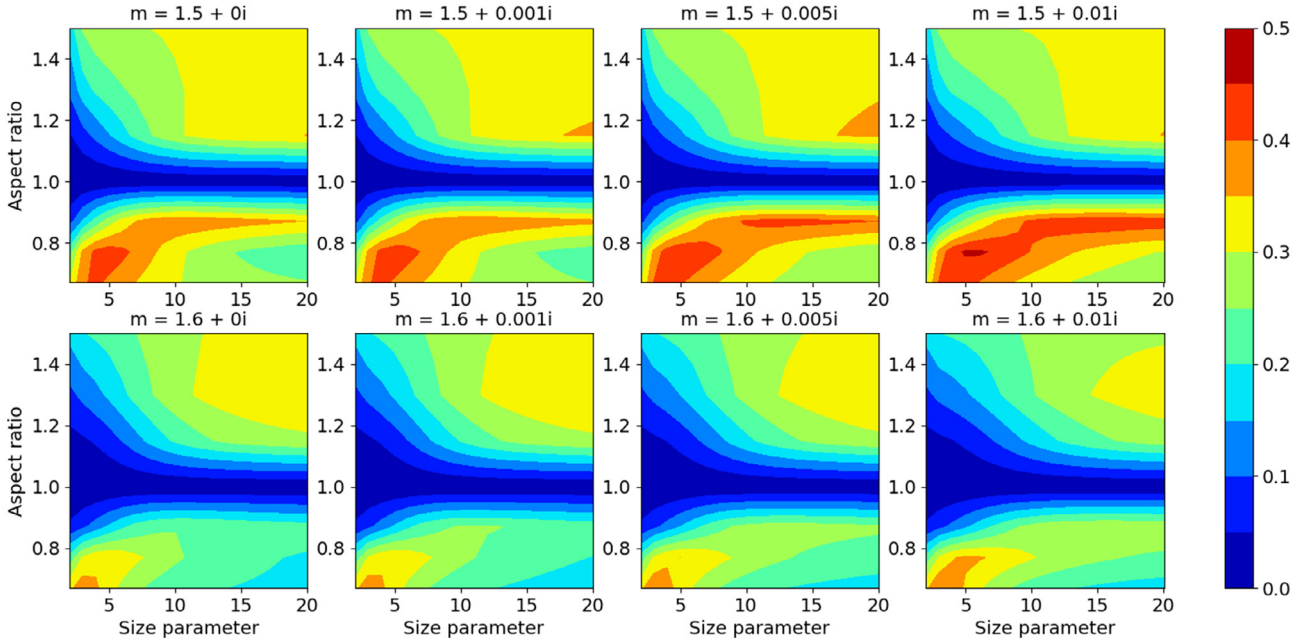

Fig. 4. Size-averaged linear depolarisation ratio in the exact backscattering direction, modelled for randomly oriented homogeneous spheroids. The results are shown as a function of the median size parameter x_0 and aspect ratio a/b. The eight panels show results for different refractive indices, as indicated in each panel heading.

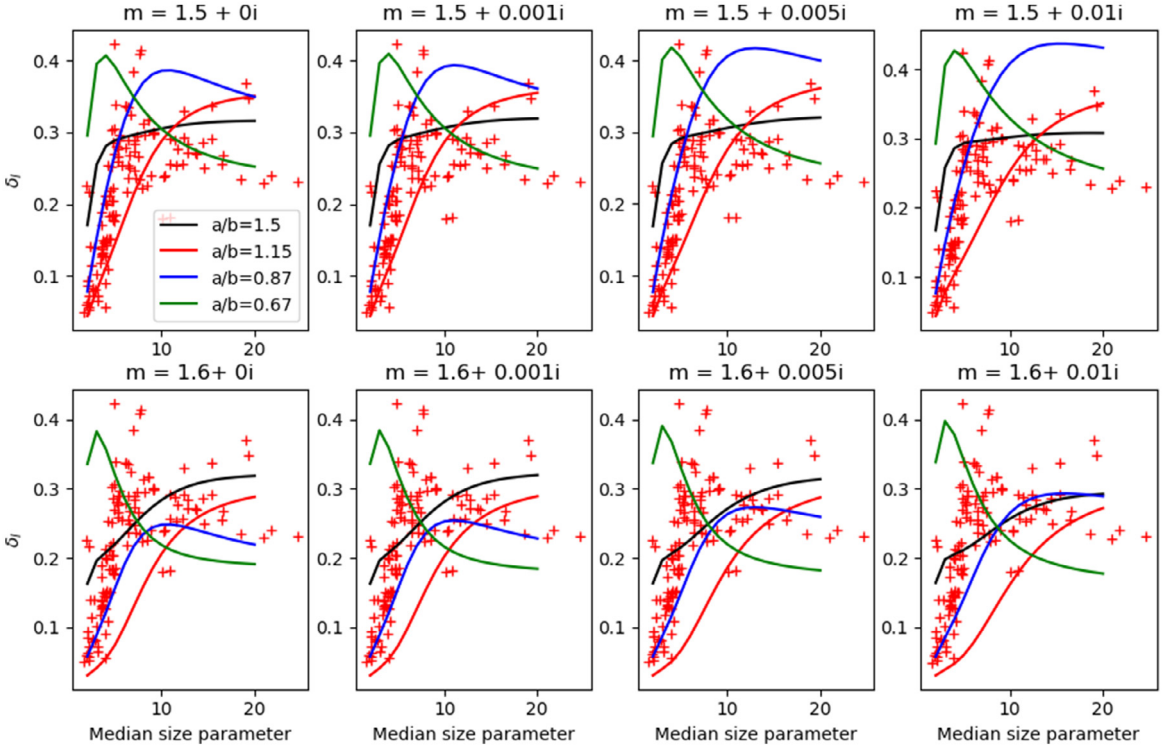

Fig. 5. Depolarisation as a function of median size parameter. The panels are as in Fig. 4. The curves show computational results extracted from SCATDB, as in Fig. 4, but only for selected spheroid aspect ratios (as indicated in the legend). The measurements are represented by pluses.

and the standard deviation

$$\sigma_\delta = \sqrt{\frac{1}{N}\sum_{i=1}^{N}(\delta_i^{\mathrm{obs}} - \delta_i^{\mathrm{mod}})^2}, \tag{8}$$

where δ_i^{obs} and δ_i^{mod} denote observed and modelled depolarisation ratios, respectively, and where the sum extends over all measurements labeled by i. The model results were computed for median size parameters x_0=1, 2, …, 20 and linearly interpolated to the corresponding size parameters of the observed aerosol samples.

Fig. 6 shows the bias (left) and standard deviation (centre column) as a function of the real and imaginary parts of the refractive index computed for aspect ratios a/b=0.93 (top), 0.87 (centre row), and 0.77 (bottom). It is evident that the bias and variance are smallest for an aspect ratio of a/b=0.87. The minimum bias is reached around a real part of the refractive index of n=1.525; it is

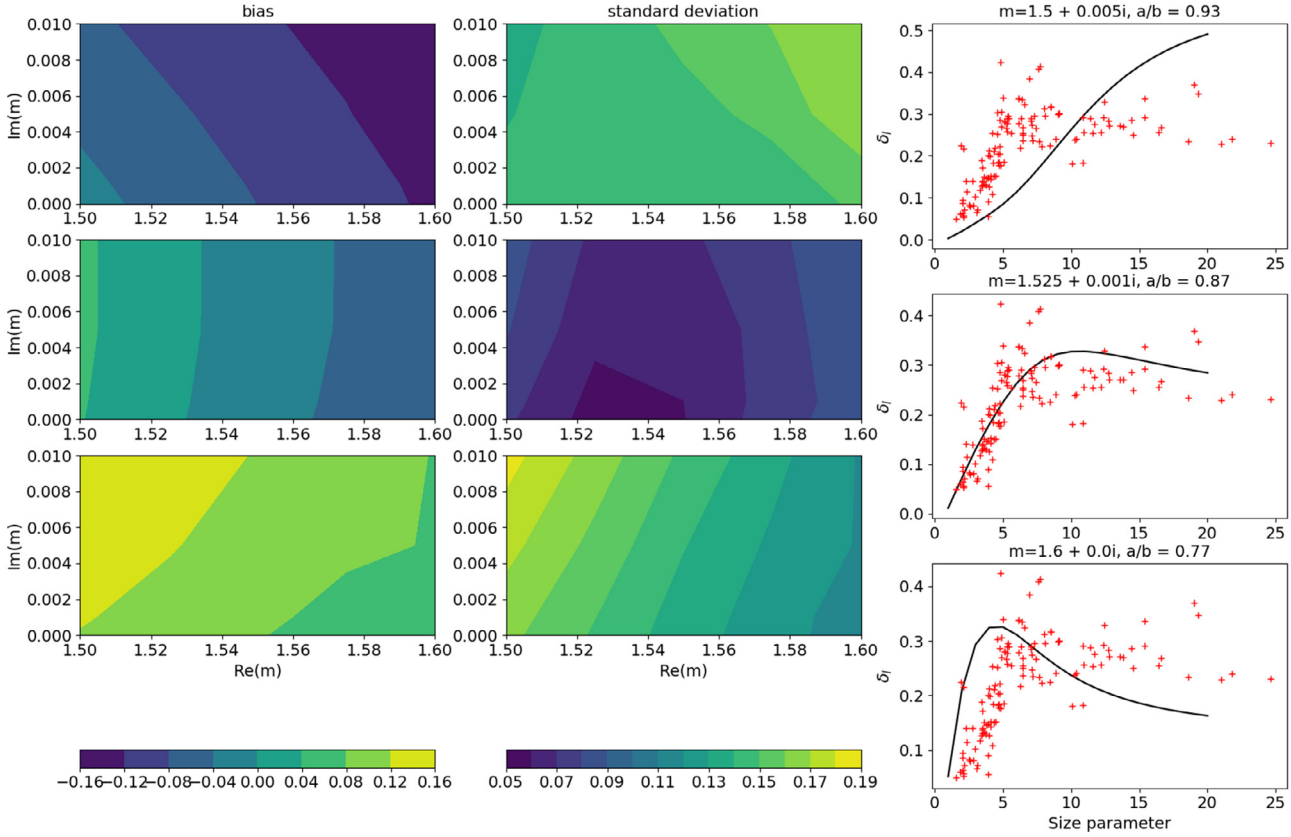

Fig. 6. Bias (left) and standard deviation (centre column) as a function of the real and imaginary part of the refractive index, obtained by comparing the observations with spheroids with aspect ratios a/b=0.93 (top), 0.87 (centre row), and 0.77 (bottom). The right column shows the size dependence of the data (pluses) and model (solid line) for the three different aspect ratios, choosing in each case that refractive index that minimises the standard deviation.

nearly independent of κ. The standard deviation is smallest around n=1.525 and κ between 0 and 0.001. The right column shows the data points and the modelled depolarisation ratio for a/b=0.93, m=1.5 + 0.005i (top), a/b=0.87, m=1.525 + 0.001i (centre), and for a/b=0.77, m=1.6 + 0.0i. Each curve represents the minimum-variance solution for each aspect ratio. For a/b=0.87 we obtain the best fit of the data.

3.3. Estimating the model uncertainty

After we had found a model that reproduces the mean trend in the measurements, we wanted to quantify the contribution of different sources of uncertainty to the spreading of the data points. We considered five possible error sources, namely, (i) uncertainty in the refractive index, (ii) variation in the geometric standard deviation of the size distribution, (iii) variation in the aspect ratio, (iv) irregular distortions of the ideal spheroidal geometry, and (v) inhomogeneous mineralogical composition. The results of this error analysis are shown in Fig. 7. In all panels, the measurements are represented by red pluses, and the reference model (homogeneous spheroids with a/b=0.87, m=1.525 + 0.001i, $\sigma_{\rm n}$ given in Eq. (5)) is shown as a black line.

1. Upper left: Optical properties of prolate spheroids with an aspect ratio of a/b=0.87 have been computed for different refractive indices. The real part was varied between 1.50 to 1.55, and the imaginary part between 0.0 and 0.005. The maximum variation of the modelled linear depolarisation ratio at 178° is indicated by the shaded region.
2. Upper right: The geometric standard deviation of the size distribution was varied between $\sigma_n(x_0) - \sigma_s$ and $\sigma_n(x_0) + \sigma_s$, where σ_s=0.214 (see discussion in Sect. 3.1 and Fig. 3). The aspect ratio of the spheroids and the refractive index were fixed at the reference values. The resulting maximum variation in the modelled linear depolarisation ratio is indicated by the shaded region.
3. Centre left: We saw in Fig. 4 that a variation in the aspect ratio can give rise to a substantial variation in the depolarisation ratio that far exceeds the spreading of the observations. Thus, to assess the sensitivity of δ_l to a variation to the overall shape of the particle, we varied the aspect ratio only within a narrow range between 0.77 and 0.93, while keeping the refractive index and the geometric standard deviation fixed at the reference values. The maximum range within which the computational results vary is indicated by the shaded region.
4. Centre right: Deviations from an ideal spheroidal shape were explored by super-imposing Gaussian random distortions to spheroids with a fixed aspect ratio of 0.87, as explained in Sect. 2.2. The shaded region in the centre right panel indicates the mean ± one standard deviation, where the ensemble, for each size, was composed of 25 different randomly distorted geometries. Results for the entire ensemble of Gaussian random spheroids are shown in Fig. 8. The legend indicates five classes of rough spheroids which, from top to bottom, correspond to the particles shown from left to right in Fig. 1. For each class of Gaussian random spheroids, the figure shows results for five stochastic realisations of the randomised geometry. We see that morphological irregularity accounts for a considerable spread of the modelled depolarisation ratios about the results obtained for the homogeneous reference spheroids. Any single one of these five classes of Gaussian random spheroids could give a biased error estimate. For instance, the one with $\sigma_{\rm r}$=0.03, γ =

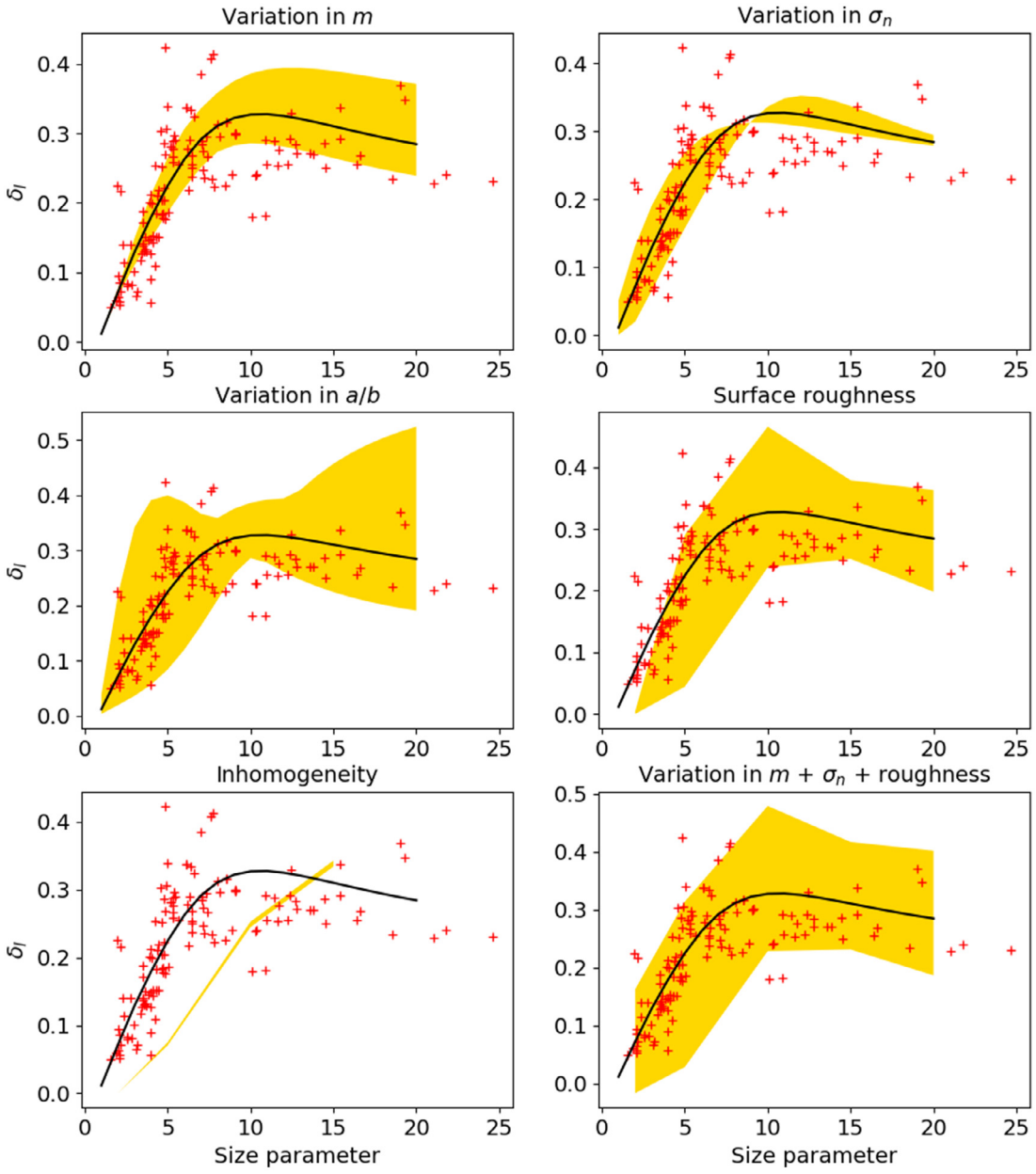

Fig. 7. Model variability (represented by the shading) due to variation in refractive index (top left), geometric standard deviation of the size distribution (top right), aspect ratio (centre left), surface roughness (centre right), and inhomogeneous composition (bottom left). The bottom right panel shows the first, second, and fourth error sources combined.

20° tends to underestimate depolarisation for $x \leq 10$, and overestimate depolarisation for $x > 15$. Only the entire ensemble consisting of different roughness models and stochastic realisations yields a reasonably even spread of the computational results about the reference curve. For $x = 2$, irregularity only results in a negative bias relative to the reference results.

5. Bottom left: We replaced homogeneous spheroids with inhomogeneous spheroids containing randomly placed hematite inclusions, as explained in Section 2.2. The shaded region shows the ensemble mean $\pm$ one standard deviation, where the ensemble consisted of 10 random realisations of the inhomogeneous morphology. We see that inhomogeneity gives rise to very little variability, although it can introduce quite a bias.
6. Bottom right: Neglecting inhomogeneity and variation in the aspect ratio, we estimated the total error as follows. We calculated for each size $s^i_+ = \delta^i_+ - \delta_{ref}$ and $s^i_- = \delta^i_- - \delta_{ref}$, where $\delta_{\rm ref}$ is the depolarisation computed with the reference model, $i = 1, 2, 3$ labels variation in m, σ_n, and surface roughness, respectively, and δ^i_+, δ^i_- are the corresponding upper and lower bounds indicated by the yellow shadings. Assuming that these errors are uncorrelated, we computed, for each size, the standard deviation of all error sources:

$$\sigma_{\text{total},+} = \sqrt{\sum_{i=1}^{N} {s^i_+}^2} \tag{9}$$

$$\sigma_{\text{total},-} = \sqrt{\sum_{i=1}^{N} {s^i_-}^2}. \tag{10}$$

The resulting range is shown in the figure.

Note that the error estimates for irregularity (centre right) and inhomogeneity (bottom left) have been modelled differently from the others. For variations in m, $\sigma_{\rm n}$, and a/b we prescribed a maximum range of variation. For the extreme values of these ranges, we

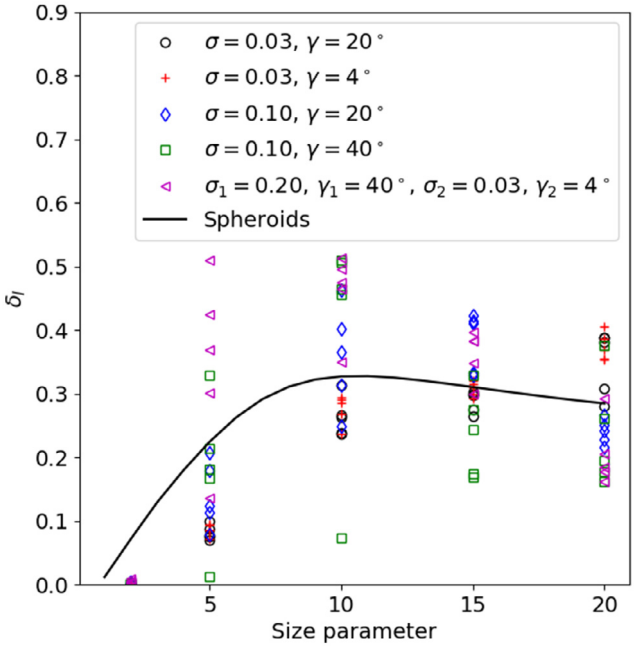

Fig. 8. Linear depolarisation ratio at a scattering angle of 178° as a function of size parameter, computed for the reference lognormal size distribution of spheroids (solid line), and for different monodisperse Gaussian random spheroids (as indicated in the legend). For each roughness scale, five stochastic realisations of the randomised geometry were computed.

computed size-averaged optical properties of spheroids for each value of the median size parameter x_0, and we took the resulting maximum variation of the depolarisation within each parameter range as our error estimate. By contrast, DDA computations for irregular and inhomogeneous particles are prohibitively expensive for such an approach. Instead, we computed optical properties for particles of a single size, but for a stochastic ensemble at each size. The error estimates were obtained by computing the standard deviation of the ensemble at each size. We then invoked the assumption that this method gives us a viable error estimate for size-averaged depolarisation ratios.

3.4. Fitting AIDA data with a shape distribution of spheroids

Our approach, so far, was to identify a single spheroidal shape that reproduces the observations. This gave remarkably satisfactory results. However, in other studies one has employed distributions of aspect ratios, e.g., to construct kernels for remote sensing retrieval methods [25], or for fitting the Mueller matrix elements of mineral dust particles [26]. The statistical weights that each spheroidal shape (i.e., aspect ratio) have in the ensemble are free parameters. The main idea in such an approach is to increase the number of free parameters in order to fit multiple optical parameters or optical parameters at multiple wavelengths. Here, we make no attempt to fit optical parameters other than the depolarisation ratio. However, we want to briefly address the question whether or not we have some flexibility in specifying the weights in a shape distribution of aspect ratios. A glance at Fig. 4 suggests that only a fairly narrow range of aspect ratios is likely to provide a good fit of δ_l as a function of size parameter.

We tested this approach by keeping the refractive index fixed at m=1.525+0.001i. The shape distribution contained nine discrete aspect ratios in the range $0.5 \le a/b \le 2.0$. We determined the statistical weights of the aspect ratios in the size-shape distribution of spheroids by least-squares fitting of the depolarisation measurements. The result of this exercise depends on the a priori shape distribution that is provided to the least-squares minimisation routine. We tested three different a prioris, which correspond to the three rows in Fig. 9.

- Knowing that spheroids with a/b=0.87 provide a good fit of data, we set the weights $w(a/b)$ such that $w(0.87)$=0.6 and $w(a/b) = 0.05$ for the remaining eight aspect ratios.
- For the second a priori, we used an equi-probable shape distribution with $w(a/b) = 1/9$ for all aspect ratios.
- For the third a priori, we used the so-called $|\xi|^3$ shape distribution [20]. The idea is to map the aspect ratio onto a linear scale by introducing the shape parameter [48]

$$\xi = \begin{cases} 1 - b/a & : \quad a/b < 1 \text{ (prolate)} \\ a/b - 1 & : \quad a/b \ge 1 \text{ (oblate)} \end{cases} \tag{11}$$

and to define a shape distribution

$$w(\xi) \propto |\xi|^3. \tag{12}$$

This distribution puts more weight on those aspect ratios that deviate more strongly from spherical shape, which proved to be particularly useful in reproducing the asymmetry parameter of mineral dust aerosols [26].

For the first a priori (Fig. 9, top row) we obtain a fit of the data (solid line) that is almost equally good as for a single spheroidal aspect ratio (dotted line). The model slightly overestimates the data for size parameters $x \le 5$, and it gives somewhat low depolarisation ratios for $x \ge 15$. We also see that the fitting result and the a priori are almost indistinguishable.

For the equi-probable a priori (middle row), the fit significantly improves the a priori, and is generally equally good as the fit we previously obtained with a single aspect ratio (left). For size parameters around 10, the fit of the data is even slightly better than for a single spheroid (compare the solid and the dotted lines). The best-fit shape distribution (right) contains both prolate and oblate spheroids that do not deviate much from spherical shape; $w(0.87)$ and $w(1.15)$ are almost equally large.

For the $|\xi|^3$ a priori we do not obtain a satisfactory fit of the data (left). The least-squares fitting routine yields a shape distribution (right) that is strongly dominated by highly aspherical prolate spheroids with $a/b = 0.5$.

4. Discussion

Comparison of field measurements in Tab. 1 and the results presented here (e.g. in the bottom right panel of Fig. 7) shows that for size parameters larger than about 7 the field observations, laboratory measurements, and model results are largely consistent within the variance of the model and the AIDA data. However, both the AIDA measurements and the model output indicate that populations of mineral dust aerosols with median size parameters smaller than 7 can have depolarisation ratios significantly smaller than those that are typically observed in the field.

Our sensitivity study suggests that particle morphology is the main contributor to the variability of depolarisation among different mineral dust samples, followed by the uncertainty in the refractive index. On the other hand, the geometric standard deviation of the size distribution contributes little to the total error variance of the model results.

A closer inspection of the aerosols samples studied in the AIDA chamber has been performed in [34]. Many of the dust samples display irregular shapes and surface roughness (see Fig. 3 in [34]). However, there is no clear trend that certain types of samples or certain morphological characteristics give rise to consistently higher or lower depolarisation ratios (see Fig. 7 in [34]). For instance, for size parameters larger than about 8 both volcanic ash particles and Sahara dust aerosols have depolarisation ratios that

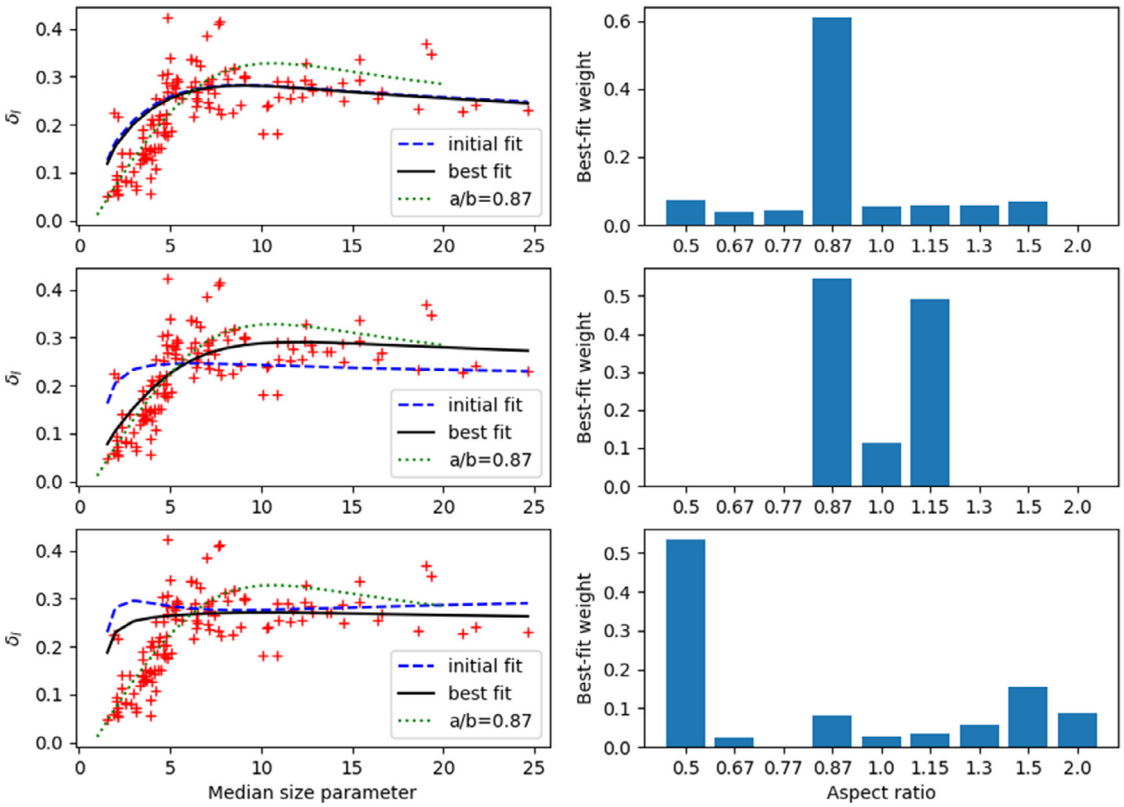

Fig. 9. Left column: linear depolarisation ratio at a scattering angle of 178° as a function of size parameter, fitted with a shape-distribution of homegeneous spheroids. The plots show the measurements (pluses), a priori (dashed line), and least-squares fit (solid line), as well as the best model results obtained by using a single spheroid of a/b=0.87 (dotted line). Right column: best-fit weights of the spheroid aspect ratios in the shape distribution. The three rows show results obtained for three different a priori shape distributions used in the least-squares minimisation routine, as explained in the text.

scatter fairly uniformly about a mean value of ~ 0.3. This indicates that complex morphological features generally do result in a random error, rather than giving rise to systematic signatures in the depolarisation ratio.

Our model results for particles with inhomogeneous composition seem to be, at first glance, the exception to this rule. However, it is difficult to draw definite conclusions based on the results we obtained for inhomogeneous particles. Earlier studies have shown that randomly placed inhomogeneous hematite inclusions inside a quartz matrix can give rise to significant uncertainties in modelled depolarisation ratios [6]. By contrast, our results suggest that inhomogeneity may introduce a bias, but it does not give rise to much variance in the modelled depolarisation ratio. The main difference is that in [6] the hematite volume fractions were as high as 4%. Here, we considered a volume fraction of only 0.74%, because application of effective medium theory with this volume fraction yields an effective refractive index consistent with that of the best-fit spheroids. For such low volume fractions we had little freedom in varying the inclusion size. Random variations in the placement of the hematite inclusions did not result in much variation in the modelled depolarisation ratio.

Our results also illustrate an important aspect of spheroids, and, indeed, of simplified model particles in general. In [49] it has been explained that a versatile simple model particle needs to have the following properties.

(i) It simplifies the morphology as much as possible (without over-simplifying it);
(ii) it has a small number of free tuning parameters;
(iii) it covers a large range of optical properties by varying the tuning parameter; and
(iv) it is capable of reproducing several optical parameters for a range of particle sizes, wavelengths, and compositions.

The versatility of spheroids in our case is, indeed, based on their geometric simplicity, and on their property of covering a large range of depolarisation ratios by varying a single parameter, the aspect ratio a/b (see Fig. 4). However, the very same property makes it also problematic to employ spheroids for estimating the error variance of the model, which is needed for inverse modelling. Varying a/b over a large range will result in error estimates that are much larger than those observed in the measurements. We addressed this issue by drastically reducing the range over which we varied the aspect ratio. Even so, a variation in a/b still results in uncertainty estimates that exceeds the spreading of the data points, particularly for large size parameters (see the centre left panel in Fig. 7). Further, we see in Fig. 7 that a variation in a/b can give conspicuously looking features in the error estimates, such as a maximum at size parameters around $x = 5$ and a minimum around $x = 10$. These features are absent in the scattering of the measurements. Owing to these issues specific to spheroids, we attempted to obtain an estimate of the total model error (bottom right panel of Fig. 7) by only accounting for the variations in the refractive index, the geometric standard deviation of the size distribution, and for the effect of surface roughness. In the absence of measurements to guide us, it may be very difficult to employ spheroids, or any simple model particle satisfying item (iii) above, for obtaining meaningful error estimates. In such case, the use of complex, morphologically realistic model particles with stochastically varying properties may be the only viable approach for obtaining meaningful error estimates (see the centre right panel in Fig. 7).

Further, we saw in Fig. 8 that the use of stochastically varying shapes needs to proceed with some caution in order to avoid biased error estimates. In our case, we saw that we need to employ both different roughness models and different stochastic realisations for each model in order to obtain an even spread of the computational results about the reference model.

Finally, we attempted to fit the depolarisation ratio with an ensemble of aspect ratios, instead of a single aspect ratio. We learn from this test that we have a certain freedom in choosing a shape-distribution of spheroids. This flexibility could, perhaps, be exploited when we want to fit, e.g., depolarisation at multiple wavelengths, or multiple optical parameters. However, the results also suggest that this freedom is more limited than one may have expected. A good fit of the measurements with the model is mostly obtained for those ensembles that are dominated by spheroids that deviate only mildly from spherical shape. This trend can present a challenge when attempting to model various optical properties simultaneously. For instance, in attempts of fitting the Mueller matrix or representing the asymmetry parameter of mineral dust, the opposite trend has been noted. Those ensembles of spheroids that place much weight on more strongly aspherical oblate or prolate spheroids have frequently given the best results (e.g. [21,26,48]).

It also became clear that the result of fitting the data with a distribution of aspect ratios is strongly dependent on the a priori. This indicates that the use of the Levenberg-Marquardt minimisation method may not be the best choice for this kind of problem; a global minimisation method may give more robust results. However, the salient point of this test was the limited flexibility in adapting the distribution of aspect ratios. This conclusion has little to do with the choice of the minimisation method. It is a consequence of the fact that only a narrow range of mildly aspherical spheroids display a dependence of δ_l on size parameter that resembles that of the observations, as we already saw in Fig. 4.

5. Summary and conclusions

The main goal of this work was to find a simple model that reproduces the size dependence of the linear depolarisation ratio of mineral dust aerosols observed in the AIDA chamber. The observations comprised measurements on 131 samples with different size distributions, mineralogical compositions, and morphology. We considered spheroidal model particles with size distributions that were modelled after the measured samples. We varied the aspect ratio and the complex refractive index of the model over a considerable range in order to search for a best fit.

We were able to identify a spheroid model that yields a minimum-bias and minimum-variance fit of the observed depolarisation ratio at a scattering angle of 178°. The best-fit spheroids are prolate with an aspect ratio of a/b=0.87 and a refractive index of m=1.525+0.001i. The variation of the observations about the mean can be explained by a variation in morphology and dielectric properties, and to a much lesser degree by uncertainties in the geometric variance of the lognormal size distribution.

These results confirm the well-known fact that spheroids are a flexible model for reproducing optical properties of mineral aerosols [20,21,25,26], including differential radiometric and polarimetric properties. This particular strength of the spheroid model derives from the fact that by varying the aspect ratio one can cover a large range of optical properties [24]. However, the very same property makes it difficult to employ spheroids for estimating the model uncertainty. A change in the aspect ratio resulted in variations in the depolarisation ratio over a range that far exceeded that of the observations. It is conceivable that this weakness becomes even more pronounced in this particular approach, in which we fitted the measurements by use of a *single* aspect ratio.

We also saw that error estimates based on varying a single property of the model particles can give conspicuously looking error estimates that do not well agree with the observed scattering of the data points. In order to obtain an error estimate that was both qualitatively and quantitatively realistic, we had to compute a geometric mean error variance over different error sources, namely, a morphological variation represented by different models of Gaussian random surface deformations, a variation in the refractive index, and a variation in the geometric mean of the size distribution.

Finally, we studied the prospects of fitting the AIDA data with an ensemble of aspect ratios, instead of using a single aspect ratio. The motivation of introducing such a shape-ensemble is to increase the number of degrees of freedom, which could be useful when attempting to reproduce depolarisation at multiple wavelengths, or multiple optical properties. We found, indeed, that we have a certain flexibility in specifying the statistical weights of the aspect ratios, but not as much as one may expect. Aspect-ratio distributions of spheroids that gave a reasonably good fit of the measured depolarisation ratios tended to be confined to only mildly aspherical prolate and oblate spheroids.

Declaration of Competing interest

The authors declare that they have no known competing financial interests or personal relationships that could have appeared to influence the work reported in this paper.

Acknowledgments

We are grateful to Karri Muinonen and Timo Nousiainen for making the G-sphere program freely available, to Michael Mishchenko for publishing his T-matrix program, to Bruce Draine and Piotr Flatau for publishing the DDSCAT code, and to Maxim Yurkin and Alfons Hoekstra for making their ADDA code publicly available. We further acknowledge funding by the Swedish National Space Agency *Rymdstyrelsen* under contract 100/16 (MK) and by the Swedish Research Council (Vetenskapsrådet) under contract 2016-03499 (FK).

References

[1] Waquet F, Cairns B, Knobelspiesse K, Chowdhary J, Travis LD, Schmid B, et al. Polarimetric remote sensing of aerosols over land. J Geophys Res 2009;114:D1.
[2] Generoso S, Bréon F-M, Chevallier F, Balkanski Y, Schulz M, Bey I. Assimilation of POLDER aerosol optical thickness into the LMDz-INCA model: implications for the arctic aerosol burden. J Geophys Res 2007;112:D2.
[3] David G, Thomas B, Nousiainen T, Miffre A, Rairoux P. Retrieving simulated volcanic, desert dust and sea-salt particle properties from two/three-component particle mixtures using UV–vis polarization lidar and t matrix. Atmos Chem Phys 2013;13:6757–76.
[4] Mehri T, Kemppinen O, David G, Lindqvist H, Tyynel J, Nousiainen T, et al. Investigating the size, shape and surface roughness dependence of polarization lidars with light-scattering computations on real mineral dust particles: application to dust particles external mixtures and dust mass concentration retrievals. J Atmos Res 2018;203:44–61.
[5] Lindqvist H, Jokinen O, Kandler K, Scheuvens D, Nousiainen T. Single scattering by realistic, inhomogeneous mineral dust particles with stereogrammetric shapes. Atmos Chem Phys 2014;14:143–57.
[6] Kahnert M. Modelling radiometric properties of inhomogeneous mineral dust particles: applicability and limitations of effective medium theories. J Quant Spectrosc Radiat Transf 2015;152:16–27.
[7] Kanngießer F, Kahnert M. Calculation of optical properties of light-absorbing carbon with weakly absorbing coating: a model with tunable transition from film-coating to spherical-shell coating. J Quant Spectrosc Radiat Transf 2018;216:17–36.
[8] Kahnert M, Andersson E. How much information do extinction and backscattering measurements contain about the chemical composition of atmospheric aerosol. Atmos Chem Phys 2017;17:3423–44.
[9] Omar AH, Winker DM, Vaughan MA, Hu Y, Trepte CR, Ferrare RA, et al. The CALIPSO automated aerosol classification and lidar ratio selection algorithm. J Atmos Ocean Technol 2009;26:1994–2014.

[10] Burton SP, Hair JW, Kahnert M, Ferrare RA, Hostetler CA, Cook AL, et al. Observations of the spectral dependence of particle depolarization ratio of aerosols using NASA langley airborne high spectral resolution lidar.. Atmos Chem Phys 2015;15:13453–73.
[11] Groß S, Tesche M, Freudenthaler V, Toledano C, Wiegner M, Ansmann A, et al. Characterization of Saharan dust, marine aerosols and mixtures of biomass-burning aerosols and dust by means of multi-wavelength depolarization and raman lidar measurements during SAMUM 2. Tellus B 2011;63(4):706–24.
[12] Ancellet G, Pelon J, Totems J, Chazette P, Bazureau A, Sicard M, et al. Long-range transport and mixing of aerosol sources during the 2013 North American biomass burning episode: analysis of multiple lidar observations in the western mediterranean basin. Atmos Chem Phys 2016;16(7):4725–42. doi:10.5194/acp-16-4725-2016.
[13] Murayama T, Müller D, Wada K, Shimizu A, Sekiguchi M, Tsukamoto T. Characterization of Asian dust and Siberian smoke with multiwavelength Raman lidar over tokyo, japan in spring 2003. Geophys Res Lett 2004;31:L23103.
[14] Burton SP, Ferrare RA, Hostetler CA, Hair JW, Rodgers RR, Obland MD, et al. Aerosol classification using airborne high spectral resolution lidar measurements — methodology and examples. Atmos Meas Tech 2012;5:73–98.
[15] Tesche M, Gross S, Ansmann A, Müller D, Althausen D, Freudenthaler V, et al. Profiling of saharan dust and biomass-burning smoke with multiwavelength polarization raman lidar at cape verde. Tellus B 2011;63(4):649–76.
[16] Bohlmann S, Baars H, Radenz M, Engelmann R, Macke A. Ship-borne aerosol profiling with lidar over the atlantic ocean: from pure marine conditions to complex dust–smoke mixtures. Atmos Chem Phys 2018;18(13):9661–79.
[17] Ansmann A, Rittmeister F, Engelmann R, Basart S, Jorba O, Spyrou C, et al. Profiling of Saharan dust from the Caribbean to western Africa – Part 2: shipborne lidar measurements versus forecasts. Atmos Chem Phys 2017;17(24):14987–5006.
[18] Hofer J, Althausen D, Abdullaev SF, Makhmudov AN, Nazarov BI, Schettler G, et al. Long-term profiling of mineral dust and pollution aerosol with multiwavelength polarization raman lidar at the central asian site of dushanbe, tajikistan: case studies. Atmos Chem Phys 2017;17(23):14559–77.
[19] Muñoz O, Moreno F, Guirado D, Dabrowska DD, Volten H, Hovenier JW. The Amsterdam-Granada light-scattering database. J Quant Spectrosc Radiat Transf 2012;113:565–74.
[20] Kahnert M, Nousiainen T, Veihelmann B. Spherical and spheroidal model particles as an error source in aerosol climate forcing and radiance computations: a case study for feldspar aerosols. J Geophys Res 2005;110:D18S13.
[21] Nousiainen T, Kahnert M, Veihelmann B. Light scattering modeling of small feldspar aerosol particles using polyhedral prisms and spheroids. J Quant Spectrosc Radiat Transf 2006;101:471–87.
[22] Veihelmann B, Nousiainen T, Kahnert M, van der Zande WJ. Light scattering by small feldspar particles simulated using the gaussian random sphere geometry. J Quant Spectrosc Radiat Transf 2006;100(1–3):393–405.
[23] Merikallio S, Nousiainen T, Kahnert M, Harri AM. Light scattering by the martian dust analog, palagonite, modeled with ellipsoids. Opt Express 2013;21:17972–85.
[24] Nousiainen T, Kahnert M, Lindqvist H. Can particle shape information be retrieved from light-scattering observations using spheroidal model particles? J Quant Spectrosc Radiat Transf 2011;112:2213–25.
[25] Dubovik O, Sinyuk A, Lapyonok T, Holben BN, Mishchenko MI, Yang P, et al. Application of spheroid models to account for aerosol particle nonsphericity in remote sensing of desert dust. J Geophys Res 2006;111:D11208.
[26] Merikallio S, Lindqvist H, Nousiainen T, Kahnert M. Modelling light scattering by mineral dust using spheroids: assessment of applicability. Atmos Chem Phys 2011;11:5347–63.
[27] Winker DM, Vaughan MA, Omar A, Hu Y, Powell KA, Liu Z, et al. Overview of the CALIPSO mission and CALIOP data processing algorithms. J Atmos Ocean Technol 2009;26:2310–23.
[28] McGill MJ, Yorks JE, Scott VS, Kupchock AW, Selmer PA. The cloud-aerosol transport system (CATS): atechnology demonstration on the International Space Station. In: Lidar remote sensing for environmental monitoring XV, 9612. SPIE; 2015. p. 1–6.
[29] Durand Y, Hlire A, Bzy J-L, Meynart R. The ESA EarthCARE mission: results of the ATLID instrument pre-developments. In: Singh UN, Pappalardo G, editors. Lidar Technologies, Techniques, and Measurements for Atmospheric Remote Sensing III, 6750. SPIE; 2007. p. 320–32. International Society for Optics and Photonics
[30] Illingworth AJ, Barker HW, Beljaars A, Ceccaldi M, Chepfer H, Clerbaux N, et al. The EarthCARE satellite: the next step forward in global measurements of clouds, aerosols, precipitation, and radiation. Bull Amer Meteor Soc 2015;96(8):1311–32.
[31] Nousiainen T, Zubko E, Lindqvist H, Kahnert M, Tyynelä J. Comparison of scattering by different nonspherical, wavelength-scale particles. J Quant Spectrosc Radiat Transfer 2012;2012:2391–405.
[32] Schulz FM, Stamnes K, Stamnes JJ. Point group symmetries in electromagnetic scattering. J Opt Soc Am A 1999;16:853–65.
[33] Kahnert M. Irreducible representations of finite groups in the T matrix formulation of the electromagnetic scattering problem. J Opt Soc Am A 2005;22:1187–99.
[34] Järvinen E, Kemppinen O, Nousiainen T, Koiciok T, Möhler O, Leisner T, et al. Laboratory investigations of mineral dust near-backscattering depolarization ratios. J Quant Spectrosc Radiat Transf 2016;178:178–208.
[35] Schnaiter M, Büttner S, Möhler O, Skrotzki J, Vragel M, Wagner R. Influence of particle size and shape on the backscattering linear depolarisation ratio of small ice crystals — cloud chamber measurements in the context of contrail and cirrus microphysics. Atmos Chem Phys 2012;12(21):10465–84.
[36] Kahnert M, Nousiainen T, Mauno P. On the impact of non-sphericity and small-scale surface roughness on the optical properties of hematite aerosols. J Quant Spectrosc Radiat Transf 2011;112:1815–24.
[37] Kahnert M, Nousiainen T, Thomas MA, Tyynelä J. Light scattering by particles with small-scale surface roughness: comparison of four classes of model geometries. J Quant Spectrosc Radiat Transf 2012;113:2356–67.
[38] Muinonen K, Nousiainen T, Fast P, Lumme K, Peltoniemi JI. Light scattering by Gaussian random particles: ray optics approximation. J Quant Spectrosc Radiat Transf 1996;55:577–601.
[39] Kylling A, Kahnert M, Lindqvist H, Nousiainen T. Volcanic ash infrared signature: porous non-spherical ash particle shapes compared to homogeneous spherical ash particles. Atmos Meas Tech 2014;7:919–29.
[40] Mishchenko MI, Dlugach JM, Liu L. Applicability of the effective-medium approximation to heterogeneous aerosol particles. J Quant Spectrosc Radiat Transf 2016;178:284–94.
[41] Maxwell Garnett JC. Colours in metal glasses and in metallic films. Philos Trans R Soc A 1904;203:385–420.
[42] Schmidt K, Wauer J, Rother T, Trautmann T. Scattering database for spheroidal particles. Appl Opt 2009;48:2154–64.
[43] Mishchenko MI, Travis LD. Capabilities and limitations of a current FORTRAN implementation of the T-matrix method for randomly oriented, rotationally symmetric scatterers. J Quant Spectrosc Radiat Transf 1998;60:309–24.
[44] Waterman PC. Matrix formulation of electromagnetic scattering. Proc IEEE 1965;53:805–12.
[45] Mishchenko MI. Light scattering by randomly oriented axially symmetric particles. J Opt Soc Am A 1991;8:871–82.
[46] Yurkin MA, Hoekstra AG. The discrete-dipole-approximation code ADDA: capabilities and known limitations. J Quant Spectrosc Radiat Transf 2011;112:2234–47.
[47] Draine BT, Flatau PJ. Discrete-dipole approximation for scattering calculations. J Opt Soc Am A 1994;11:1491–9.
[48] Kahnert FM, Stamnes JJ, Stamnes K. Using simple particle shapes to model the Stokes scattering matrix of ensembles of wavelength-sized particles with complex shapes: possibilities and limitations. J Quant Spectrosc Radiat Transf 2002;74:167–82.
[49] Kahnert M, Kanngießer F. Modelling optical properties of atmospheric black carbon aerosols. J Quant Spectrosc Radiat Transf 2020;244:106849.